NANO LETTERS

pubs.acs.org/NanoLett Letter

Resolving Current-Dependent Regimes of Electroplating Mechanisms for Fast Charging Lithium Metal Anodes

David T. Boyle,[#] Yuzhang Li,[#] Allen Pei, Rafael A. Vilá, Zewen Zhang, Philaphon Sayavong, Mun Sek Kim, William Huang, Hongxia Wang, Yunzhi Liu, Rong Xu, Robert Sinclair, Jian Qin, Zhenan Bao,* and Yi Cui*

Cite This: https://doi.org/10.1021/acs.nanolett.2c02792 Read Online

ACCESS | Metrics & More | Article Recommendations | Supporting Information

ABSTRACT: Poor fast-charge capabilities limit the usage of rechargeable Li metal anodes. Understanding the connection between charging rate, electroplating mechanism, and Li morphology could enable fast-charging solutions. Here, we develop a combined electroanalytical and nanoscale characterization approach to resolve the current-dependent regimes of Li plating mechanisms and morphology. Measurement of Li^+ transport through the solid electrolyte interphase (SEI) shows that low currents induce plating at buried Li|SEI interfaces, but high currents initiate SEI-breakdown and plating at fresh Li|electrolyte interfaces. The latter pathway can induce uniform growth of {110}-faceted Li at extremely high currents, suggesting ion-transport limitations alone are insufficient to predict Li morphology. At battery relevant fast-charging rates, SEI-breakdown above a critical current density produces detrimental morphology and poor cyclability. Thus, prevention of both SEI-breakdown and slow ion-transport in the electrolyte is essential. This mechanistic insight can inform further electrolyte engineering and customization of fast-charging protocols for Li metal batteries.

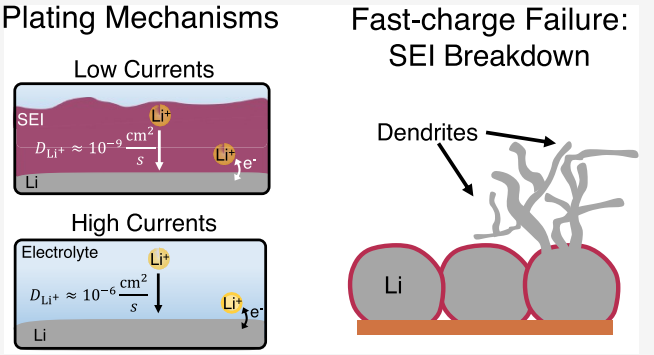

KEYWORDS: *lithium metal battery, fast charging, charge transfer, dendrite prevention, plating mechanism*

Safe and long-lasting Li metal batteries require electroplating of a uniform Li anode morphology.[1−4] Electrolyte engineering has provided a simple strategy to tune Li plating and extend the cyclability of these high-energy batteries;[4] however, most reports slowly charge the battery over 5−10 h (0.2−0.1C) to prolong cycle life.[5,6] Faster charging induces filamentary Li plating (sometimes called "dendrites"), which degrades cyclability.[1] Fully understanding the connection between the electroplating mechanism, charging rate, and Li morphology could inform development of fast charge solutions needed for practical applications, but a consensus for the current-dependence of electroplating mechanisms remains elusive.

In general, two classes of Li plating mechanisms have been discussed.[7,8] The first uses classical models describing dendritic deposition of nonreactive metals.[9−13] This class attributes large gradients of Li^+ concentration in the electrolyte during fast charging as the main cause of dendritic growth.[9,14−16] Ramified growth of Li at Sand's time (when Li^+ surface concentration reaches 0) has partially validated this idea,[17] but requisite current densities (J) generally exceed typical battery operations. Furthermore, the reactivity of Li and the solid electrolyte interphase (SEI)—a nanometers-thick and ionically conductive passivation film—are neglected. Instead, charge transfer is assumed to take place at the metal|electrolyte interface, primarily because the ionic transport properties of the SEI are not widely reported.[4,18] The second class proposes that the SEI modulates morphology. Local heterogeneities of the SEI[19−22] or SEI-fracture from volume expansion of the underlying Li[23−27] are thought to favor nonuniform morphology. *In situ* microscopy has supported this model, but observational conditions were often unrepresentative of battery operations or made without quantitative connection to the electroplating mechanism.[22,27−32] This class generally assumes that plating occurs at buried Li|SEI interfaces and Li^+ migration through the SEI is rate limiting. However, determination of whether Li plates are at buried Li|SEI interfaces is sometimes proposed to depend on J.[20,33−36] Resolving the pathways of Li plating and identifying the origin

Received: July 26, 2022
Revised: September 17, 2022

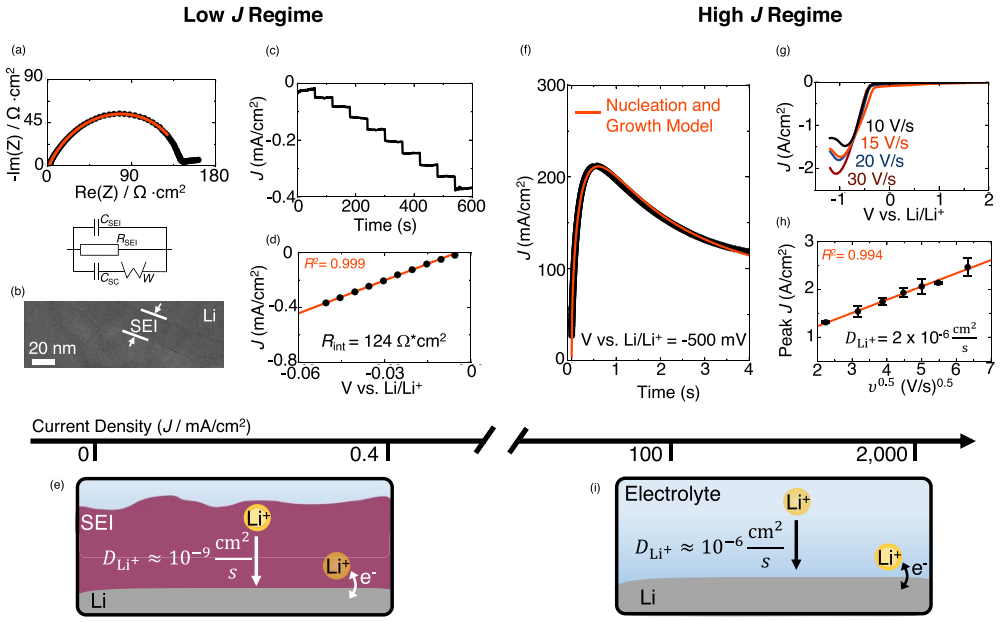

Figure 1. Pathways of Li plating within low and extremely high regimes of current. (a) Representative Nyquist plot of a Li|Li cell and equivalent circuit fit. (b) Cryo-high resolution TEM image of Li vitrified in the electrolyte shows the thickness of the SEI on Li. Because cryo-TEM images of Li vitrified in the electrolyte have very low contrast, a larger image is shown in Figure S11 to more clearly highlight the Li−SEI−electrolyte interface. (c) Current profile of Li plating in a three-electrode cell with staircase voltammetry. (d) Steady-state linear J−E relationship from (c). (e) Schematic of the electroplating pathway at low charge rates. (f) Current profile of Li plating with a −500 mV E-step and fit to a model of nonreactive metal electrodeposition. (g) LSV curves of Li plating on a tungsten UME show the relationship between peak J and E. (h) Dependence of peak current in (g) on $\upsilon^{1/2}$. (i) Schematic of the electroplating pathway at extremely fast charge rates.

Table 1. Measured Ionic Transport Properties of the SEI on Li Metal in $LiPF_6$ (EC:DEC)

d_{SEI} (nm)	R_{SEI} (Ωcm^2)	λ_{SEI} ($(\Omega cm)^{-1}$)	$D_{Li\text{-}ion}$(cm^2/s)	n_0(mol/cm^3)
20 ± 1	126 ± 13	(1.6 ± 0.2) × 10^{-8}	(2.2 ± 0.8) × 10^{-9}	(2.1 ± 0.5) × 10^{-6}

of dendritic Li morphology during fast charging are key to developing fast-charge solutions.

Here, we adapt the complementary strengths of electroanalytical and nanoscale characterization methods to establish the current-dependent regimes of Li plating and improve fast charging. We first adapt cryogenic transmission electron microscopy (cryo-TEM) to report Li^+-transport properties of the SEI. With this advance, we establish three current-dependent regimes of electroplating mechanisms that span 0.1 to about 2000 mA/cm^2. Each regime is connected to Li morphology, and we identify SEI breakdown as a primary cause of detrimental Li morphology during battery fast charging. The work provides a strategic framework to understand electroplating in batteries and guidance for improving fast-charging Li metal batteries.

Parameters describing Li^+ transport through the SEI, such as the diffusion coefficient ($D_{Li^+}^{SEI}$), ionic conductivity (λ), and carrier concentration (n_0), are critical for electroanalytically distinguishing electroplating mechanisms. To calculate these parameters, we combine EIS of Li|Li symmetric cells and cryo-TEM measurements of the native SEI thickness (Figure 1a−d). We recently deconvoluted the contribution of charge transfer and SEI resistances to the total impedance of Li metal anodes;[33] generally, >98% of the interfacial impedance corresponds to Li^+-transport through the SEI.[20,33,37] Calculation of transport parameters from EIS then requires both a reliable measurement of SEI thickness and equivalent circuit model. Vitrification of electroplated Li and its SEI and cryo-TEM imaging can preserve the native SEI thickness and enable reliable thickness measurements of the beam and air sensitive SEI.[38] TEM statistics of the SEI thickness show that the SEI thickness is about 20 nm (Figures 1b, S1). The impedance of Li with $LiPF_6$ ethylene carbonate:diethyl carbonate (EC:DEC, 1:1 by volume) electrolyte fits well to an equivalent circuit used previously to quantify Li^+ transport through a model Li_2O SEI (Figure 1a).[39] Consistent with previous measurements and simulations of Li^+ transport through model SEI,[39−42] the interfacial resistance is about 150 $\Omega \cdot cm^2$,[20] and values of $D_{Li^+}^{SEI}$ = 2.2 × 10^{-9} cm^2/s, λ = 1.6 × 10^{-8} S/cm, and n_0 = 2.1 × 10^{-6} mol/cm^3 are calculated (Table 1, *see Methods*). These parameters will serve as metrics to determine the current-dependent electroplating pathways.

EIS measurements test Li plating at the slowest possible J. To test whether ion transport through the SEI is rate limiting under more dynamic conditions, we adapt a three-electrode staircase voltammetry measurement to electroplate Li onto a Li electrode (Figure 1c, *Methods for details*). Flat steady-state J-profiles are observed for sequential E-steps increasing in magnitude from −5 mV to −50 mV. This result suggests concentration gradients in the liquid electrolyte are absent, because the J-profile would decay with time if Li^+ concentration gradients built up. The J−E plot is also ohmic with a resistance of about 124 $\Omega \cdot cm^2$ (Figure 1d). The consistency of this value with EIS suggests Li^+ transport through the SEI is rate limiting.[19,20] This result suggests plating occurs at the buried Li|SEI interface and R_{SEI} is rate limiting

https://doi.org/10.1021/acs.nanolett.2c02792
Nano Lett. XXXX, XXX, XXX−XXX

when J is less than about 0.4 mA/cm^2 (Figure 1e). Notably, such J values correspond to charging rates below 0.1C (a 10 h charge) for practical 4 mAh/cm^2 battery cathodes, which are most effective for prolonging cycle life.[5,6]

Figure 1a–d shows charge transfer occurs at the buried Li|SEI interface for low J, but several studies have suggested plating occurs at Li|electrolyte interfaces at high J.[20,33−36] These reports deposited Li at up to 2000 mA/cm^2 with ultramicroelectrodes (UME) and suggested Li plating can outpace SEI formation. Such J compared with the results in Figure 1a–d already suggests the plausibility of these claims.[23−27] Deposition of Li beneath an ohmic 100 Ω·cm^2 SEI at 2000 mA/cm^2 would require 200 V. Instead, SEI breakdown and initiation of lower impedance plating at the Li|electrolyte interface is more likely. To test this hypothesis, we expand on our previous work[33] and adapt transient linear scan voltammetry (LSV) and large E-step methods, which can electroplate Li with a J of 100–2000 mA/cm^2 and have electroanalytical utility (Figure 1f–i). Such J are outside practical ranges of battery fast charging, but resolving the plating pathway of extremely low and high J will inform analysis of the transition between them during battery relevant fast charging (discussed in Figure 3). Metrics to distinguish between electroplating pathways are the distinct ion-transport properties of the electrolyte and SEI.

Figure 1g shows a series of iR_u-compensated LSV experiments for Li plated on a tungsten UME with scan rates (υ) above 10 V/s, similar to our previous work.[33] UMEs make transient high J plating possible without distortion of the voltammogram.[43] After overcoming a nucleation barrier, J increases sharply, corresponding to the growth of Li metal, until J reaches a diffusion-limited peak (J_p). Figure 1h shows a characteristic linear relationship between $\upsilon^{1/2}$ and J_p for an irreversible electrode reaction (full details in our previous work[33]). The term irreversible here refers to the kinetic regime of the experiment and is not equivalent to its use for describing capacity loss in batteries. The effective diffusion coefficient (D_{Li^+}) can then be calculated with

$$J_p = (2.99 \times 10^5)\alpha^{1/2} C^*_{Li^+} D^{1/2}_{Li^+} \upsilon^{1/2} \quad (1)$$

where α is the transfer coefficient and $C^*_{Li^+}$ is the bulk concentration of Li$^+$.[43] Assuming α is 0.5,[33] D_{Li^+} is 2×10^{-6} cm^2/s—consistent with independent measurements of D_{Li^+} in $LiPF_6$ in EC:DEC[44,45] and 3 orders of magnitude larger than $D^{SEI}_{Li^+}$ (Table 1). This finding suggests that an SEI is not impeding Li plating and interfacial charge transfer is occurring at Li|electrolyte interfaces (Figure 1i).

To further establish that Li plating occurs at the Li|electrolyte interface at such high J, we use large E-step methods that plate Li with J > 100 mA/cm^2. Figure 1f shows a representative iR_u-corrected and three-electrode E-step experiment for Li plating at −500 mV on Cu. The J-profile fits well to a classical 3D model for the nucleation and growth of nonreactive metals developed by Scharifker (details in *methods*).[46] The fit gives values of D_{Li^+} that are again 3–4 orders of magnitude higher than $D^{SEI}_{Li^+}$, closely resembling expected values for the electrolyte[44] (Table S1). Consistency with models of nonreactive metal deposition suggest plating of new Li occurs at the Li|electrolyte interface at such high J (Figure 1e).

Previously, a similar study reported that an additional term for electrolyte reduction in the nucleation and growth model is necessary to fit the J-profile and that electrolyte reduction accounts for up to 25% of the measured current.[47] However, our data are well-described without this term. Additionally, J approaches a common value at long times for different voltage steps (Figure S2), indicating side reactions are not a major contribution to the current.[48] Discrepancies between interpretations are attributed to the extremely low capacities and short times investigated previously (~10^{-8} mAh/cm^2 and 0.2 ms)[47] compared to our measurements (~0.2 mAh/cm^2 and 5 s). While our analysis suggests the rate of concomitant electrolyte reduction is negligible compared to plating under these conditions, further exploration of the rate of electrolyte reduction on Li is necessary.

The morphological implications of the distinct electroplating pathways can inform development of strategies that tune Li morphology. Li plated in $LiPF_6$ EC:DEC at low J is generally filamentary.[1] To assess how plating at Li|electrolyte interfaces and high J influences the morphology of Li, we imaged Li plated on the UME for J ranging up to 1000 mA/cm^2 with scanning electron microscopy (SEM). For a J of 10 mA/cm^2, Li electrodeposits are expectedly filamentary (Figure 2d);

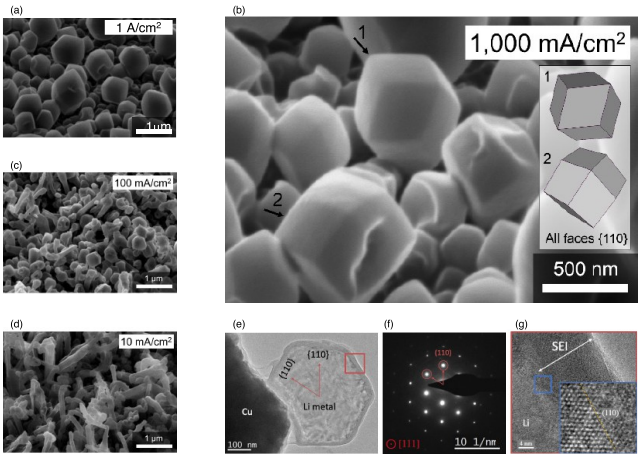

Figure 2. Plating of {110}-terminated rhombic dodecahedra shaped Li with extremely high currents. SEM images show the microstructure of electrodeposited Li metal plated at 1,000 mA/cm^2 (a,b), 100 mA/cm^2 (c), and 10 mA/cm^2 (d) on a tungsten UME. (b) SEM image showing rhombic dodecahedra of Li with clear {110}-facets. The inset of (b) shows two rhombic dodecahedron models arranged in the same orientation as two specific Li crystals highlighted with arrows (numbered 1 and 2). (e) Cryo-TEM image of faceted Li electrodeposited at 100 mA/cm^2 aligned along the ⟨111⟩ axis. (f) SAED pattern of the particle in (e) shows the characteristic SAED of BCC Li; arrows in reciprocal space are drawn in real space on (e). (g) Cryo-high resolution TEM image showing a sharp interface between a Li(110) surface and the SEI located within the red box from (e).

however, once J is 100 mA/cm^2, nonfilamentary particles emerge (Figure 2c) and above 1000 mA/cm^2 Li grows exclusively as faceted rhombic dodecahedra (Figures 2a,b, S3, S4). The rhombic dodecahedra, highlighted in Figure 2B, are characteristic of {110}-faceted body-centered cubic (BCC) crystals: {110} are the closest packed planes in BCC metals like Li.[49] This finding contradicts conventional wisdom that large gradients of Li$^+$ concentration alone during high J favor dendritic growth, suggesting the SEI plays a substantial role during real battery operation. Figure 3 explores this idea closely.

https://doi.org/10.1021/acs.nanolett.2c02792
Nano Lett. XXXX, XXX, XXX−XXX

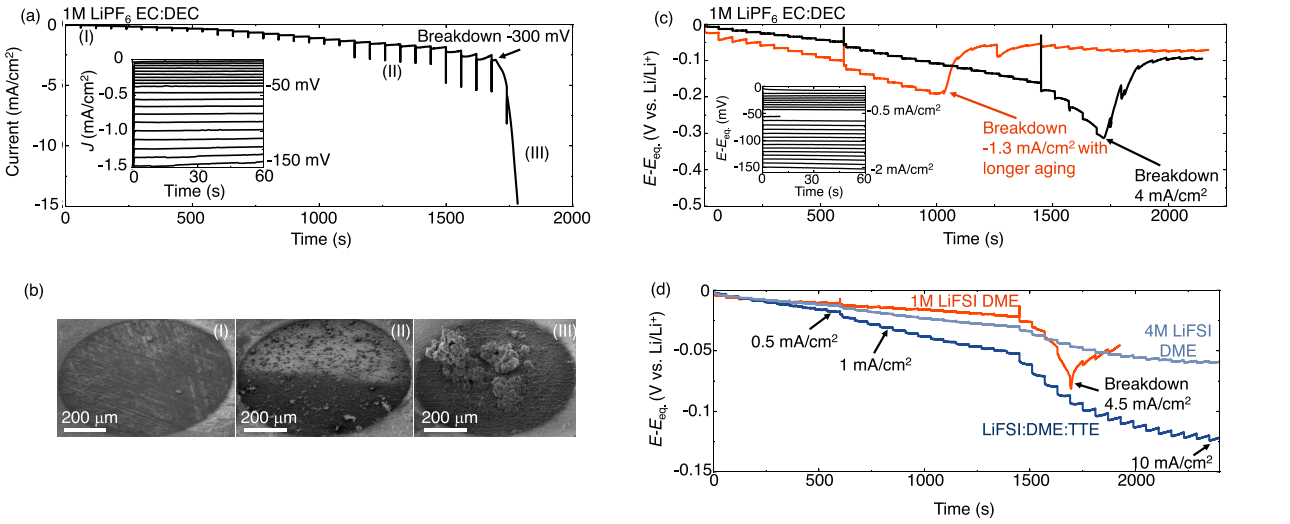

Figure 3. Breakdown of the SEI at battery-relevant fast charging rates. (a) Representative staircase voltammetry of Li electrodeposition in $LiPF_6$ EC:DEC. The inset shows the stacked *J* profiles in the low-voltage regime. (b) Representative SEM images show the morphology of Li during different stages of the staircase voltammetry measurements shown in (a). (I), (II), and (III) in the SEM images correspond to the locations highlighted in (a) and indicate where distinct measurements were stopped and taken for *ex-situ* SEM analysis. Capacities deposited during this step are 0.02, 0.8, and 1.5 mAh/cm^2, respectively. (c) Galvanostatic staircase measurements of Li electrodeposition in $LiPF_6$ EC:DEC; the inset shows the stacked voltage profiles in the low-*J* regime; black and orange lines correspond to 15 and 60 min of SEI growth, respectively. (d) Electrolyte dependence of $J_{crit.}^{SEI}$ in low and high-performance ether electrolytes.

Cryo-TEM and selected area electron diffraction (SAED) of Li plated on a Cu TEM grid at 100 mA/cm^2 confirm the indirect assessment from SEM (Figures 2e, S5). Alignment of a Li particle along the ⟨111⟩ axis (Figure 2e) gives the characteristic hexagonal SAED pattern (Figure 2f) for BCC Li crystals (space group: $Im\bar{3}m$). Arrows in the SAED pattern (Figure 2f) point along the ⟨110⟩ direction toward the reciprocal space reflections (circled in red) and correspond to the {110} family of planes. Overlaying these arrows on the Li polyhedral in Figure 2e confirms that the surfaces are {110} planes. The low surface energy and activation energy for self-diffusion on Li(110) (0.01 eV)[50] likely cause the preferential exposure. Atomic-resolution images (red box in Figure 2e) also show a well-defined atomic interface between Li(110) and an SEI (Figure 2g). The presence of an SEI here does not contradict the above discussion on high *J* plating. The SEI forms after Li plating within seconds during sample preparation. Rather, the faceted Li morphology is consistent with the electroanalytical results. Exposure of large {110} surfaces suggests plating occurs at Lillelectrolyte interfaces at such high *J*: fast surface diffusion of Li adatoms is not suppressed by an SEI. The increasing width of the particles with the capacity of electroplated Li (Figure S6) indicates growth happens at the tip rather than the base due to passivation by an SEI,[32] further supporting this picture.

Resolving the electroplating pathways at the extremes of low and high *J* enables deconvolution of the plating pathways at battery-relevant *J* (i.e., 0.4−10 mA/cm^2 or C/10 to 2.5 C for a 4 mAh/cm^2 cathode). Here, identifying the transition between regimes and whether native SEI breaks down is key. To probe this *J* regime, we expand our three-electrode staircase voltammetry method in Figure 1c,d beyond −50 mV. In Figure 3A, we sequentially step the *E* from −5 to −400 mV (*see Methods*). Low *E* gives ohmic steady-state *J*-profiles (R_{SEI} about 100 ohm·cm^2), suggesting charge transfer occurs beneath the SEI (Figure 3a inset). Once *E* reaches about −120 mV (1.2 mA/cm^2) *J* deviates from ohmic character and decays over time for a given *E* (Figure 3a inset), suggesting mixed control of *J* from R_{SEI} and Li^+ diffusion through the electrolyte. An increase in *A* would increase *J*—an opposite effect. After *E* reaches −300 mV (about 3 mA/cm^2) *J* increases sharply. This reproducible increase of *J* (Figure S7) is associated with the transition between regimes, a sharp decrease in impedance, breakdown of the SEI, and exposure of fresh Li to the electrolyte.[24] Mechanical stress from fast volume expansion of the underlying Li likely initiates the breakdown.[32]

Ex situ SEM demonstrates the morphological implication of this transition (Figure 3b). In the low *J* region (I) of Figure 3a, *ex situ* SEM shows the Li morphology is relatively uniform (Figures 3b (I), S8a). In region (II) of Figure 3a, where Li^+ diffusion through the electrolyte starts to play a role, Li plating remains mostly uniform (Figure 3b (II)). We hypothesize that some SEI-breakdown could cause Li^+ diffusion through the electrolyte to influence region (II), but the repair process is fast enough to prevent runaway growth of Li. After the SEI breaks down in region (III), high surface area Li dendrites are clearly visible (Figures 3b (III), S8b). Both filamentary and faceted particles are observed on the Li protrusions (Figure S8b). Overall, these images demonstrate that SEI breakdown initiates high surface area "dendritic" Li during battery fast charging.

J-controlled experiments are more representative of battery operations, so we developed an analogous galvanostatic staircase measurement. Figure 3c (black-line) shows the *E*-profile associated with constant current steps from 0.05 mA/cm^2 to 8 mA/cm^2. For low *J*, ohmic (R = 100 ohms·cm^2) and flat steady-state *E*-profiles are evident (Figure 3c inset). Once *J* reaches 1.5 mA/cm^2 (about −120 mV), the *E*-profile deviates from ohmic behavior and increases with time during individual *J*-steps, suggesting mixed control from SEI impedance and Li^+ transport in the electrolyte (Figure 3c inset). At 4.5 mA/cm^2 (about −300 mV), the *E* rapidly decreases, indicating the SEI

https://doi.org/10.1021/acs.nanolett.2c02792
Nano Lett. XXXX, XXX, XXX−XXX

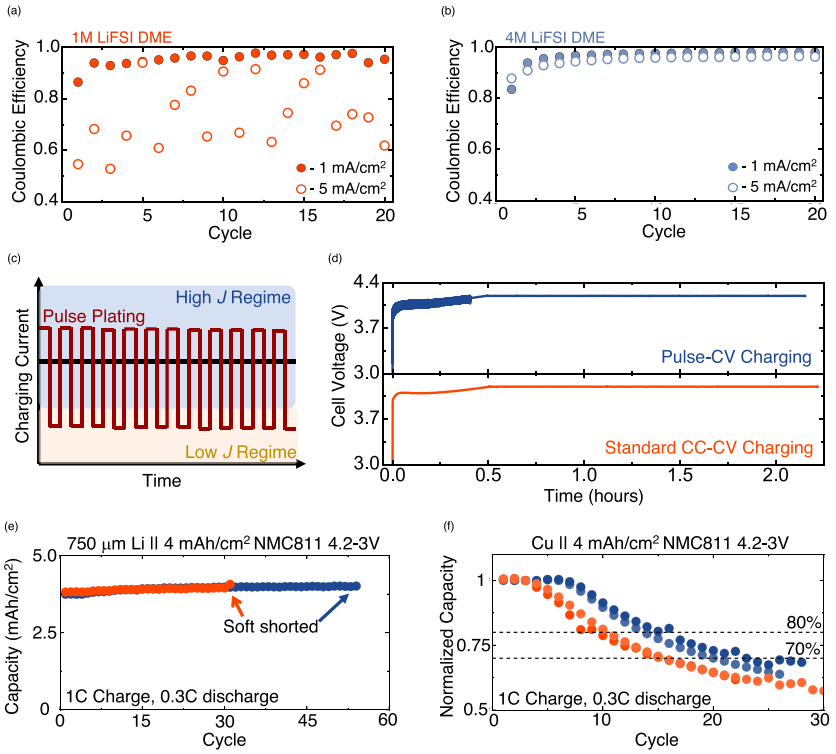

Figure 4. Implications of SEI-breakdown on cyclability and customization of fast-charging protocol. (a) Charge-rate dependent CE measurements with 1 M LiFSI in DME. (b) Charge-rate dependent CE measurements with 4 M LiFSI in DME. (c) Schematic of the proposed pulse-plating protocol alternating between high and low J regimes. (d) Representative voltage profiles for charging Li || NMC811 batteries with the pulse-CV (top) and standard CCCV (bottom) charging shows the time at the CV step and the nominal C-rate is equivalent. (e) Capacity retention of Li || NMC811 cells cycled with harsh charge−discharge rates using the pulse (blue curves) and standard (orange curves) protocol with a large excess of Li and LiFSI:DME:TTE electrolyte. Soft shorting is indicated by the corresponding voltage profiles in Figure S12. (f) Capacity retention of anode-free Li NMC811 cells cycled with harsh charge−discharge rates using the pulse (blue curves) and standard (orange curves) protocol and LiFSI:DME:TTE electrolyte.

breaks down and exposes low impedance Li surfaces. The values of J and E are consistent with the results in Figure 3a. Hence, we define J = 4.5 mA/cm^2 as a critical current density for breakdown of the SEI ($J_{crit.}^{SEI}$). Similar measurements with direct steps to J above and below $J_{crit.}^{SEI}$ verify that the breakdown is J-dependent—not capacity dependent (Figure S16).

Some studies have rationalized similar transitions between growth modes with theories using only concentration gradients in the liquid electrolyte.[17,51] There, Sand's time—when the surface concentration of Li^+ reaches 0—initiates rapid growth of Li dendrites.[17] However, Sand's time cannot explain our results. First, Sand's time only applies to constant J plating, but a transition occurs in E-step methods (Figure 3a).[43] Second, the 0.6 mAh/cm^2 of Li deposited in Figure 3c is substantially less than the calculated Sand capacity for J = 4.5 mA/cm^2, 2.1 mAh/cm^2 (see *Methods*). Lastly, aging Li for 1 h instead of the standard 15 min (*see Methods*) yields a more resistive and heterogeneous SEI[2] and decreases $J_{crit.}^{SEI}$ to 1 mA/cm^2 (Figure 3c, orange line). Hence, breakdown of the SEI, rather than ion transport in the liquid electrolyte alone, underlies the transition observed here.

$J_{crit.}^{SEI}$ also depends on the electrolyte. Figure 3d shows that a standard ether electrolyte (1 M lithium bis(fluorosulfonylimide) (FSI) in dimethoxyethane (DME)) also has a $J_{crit.}^{SEI}$ of 4.5 mA/cm^2. However, select state-of-the-art electrolytes (4 M LiFSI in DME and LiFSI:DME:2,2,3,3-tetrafluoropropyl ether (TTE)[52]) show no noticeable breakdown. We hypothesize that the nanoscale uniformity and mechanics of the compact SEI in each electrolyte are responsible for the susceptibility to SEI breakdown. State-of-the-art electrolytes form an SEI that is generally more unifom at the nanoscale and have a higher modulus than an SEI formed with $LiPF_6$ (EC:DEC) and 1 M LiFSI in DME.[38,53,54]

Coulombic efficiency (CE) measurements of Li cycled in 1 and 4 M LiFSI in DME with currents above and below $J_{crit.}^{SEI}$ for 1 M LiFSI DME demonstrate the operational importance of $J_{crit.}^{SEI}$ (Figure 4a,b). The CE quantifies Li output during battery discharge to input during.[39] Both 1 and 4 M LiFSI electrolytes give stable CE for cycles 1−20, 95.8% ± 0.5 and 96.3% ± 0.7 respectively (1 mA/cm^2, 1 mAh/cm^2). However, only the 4 M LiFSI electrolyte maintains a stable CE with 5 mA/cm^2 deposition (93.6% ± 0.9 vs 70.3% ± 2.5 for 1 M LIFSI). Hence, preventing SEI breakdown and improving ionic conductivity, the more common focus of fast charging efforts,[55] are key to fast-charging. Understanding how SEI characteristics, prior cycling, and external pressure influence $J_{crit.}^{SEI}$ will be future areas to explore. This mechanistic insight could also inform future development of custom fast-charging protocols. For example, pulse charging protocols are known to improve cyclability of Li anodes.[56−58] Pulse charging could potentially prevent the propagation of high surface area Li caused by SEI breakdown, as well (Figure 4c). Switching between slow and fast charging regimes with short pulses could prevent propagation by repairing fractured SEI during the low current density pulses. While keeping the same nominal 1C rate (Figure 4d), Figure 4e,f shows a pulse protocol alternating

https://doi.org/10.1021/acs.nanolett.2c02792
Nano Lett. XXXX, XXX, XXX−XXX

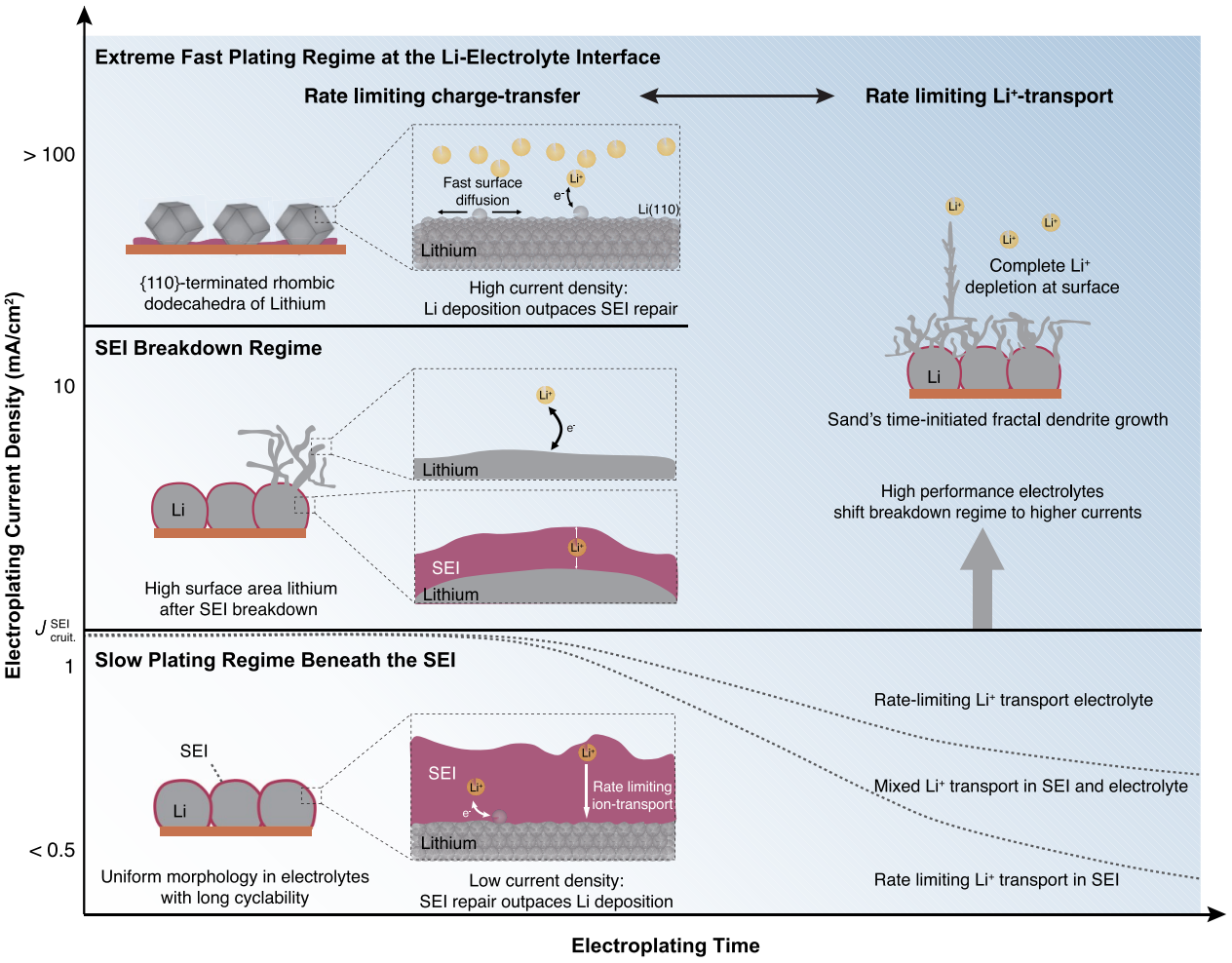

Figure 5. Current-dependent regimes of Li morphology and electroplating mechanisms.

between 1.5C and 0.05C (6 and 0.2 mA/cm^2 for 48 and 25 ms, respectively) extends the lifetime of fast-charged Li metal batteries. Optimization of the charging protocol is ongoing, but we want to introduce how mechanistic insight can inform protocols that augment electrolyte engineering.

CONCLUSIONS

This study connects the charging rate, electroplating mechanism, and morphology of Li metal anodes. Measurement of Li^+ transport through the SEI enables categorization of Li plating into three regimes (Figure 5). The slow plating regime corresponds to currents below about 1 mA/cm^2. Here, electroplating occurs at buried Lill SEI interfaces and Li^+-transport through the SEI is rate limiting. In this regime, Li morphology is more uniform, so cyclability can be extended. Currents exceeding 100 mA/cm^2 correspond to the extreme-fast plating regime. Here, electroplating fractures the SEI and occurs at fresh Lill electrolyte interfaces. Li can grow uniformly as {110}-faceted rhombic dodecahedra; however, targeting this morphology in batteries may not be ideal. Fresh Li surfaces are exposed to the electrolyte, and Sand's time could initiate fractal dendrite growth after longer charging times.

The SEI-breakdown regime is most applicable for battery fast charging. Here, SEI breakdown at about 2−4 mA/cm^2 in standard carbonate electrolyte initiates plating at fresh Lill electrolyte interfaces. Breakdown initiates dendritic Li plating and substantial loss of rechargeability. Poor ionic conductivity of the electrolyte can also favor undesirable Li morphology, but SEI breakdown presents a more extreme failure mode. Hence, mitigating SEI breakdown, in addition to improving the ionic conductivity of electrolytes, is essential for fast charging. Designing a custom charging protocol informed by this mechanism could also improve fast charging. Overall, our work highlights the power of combining electroanalytical methods with nanoscale characterization to understand complex electrochemical reactions.

ASSOCIATED CONTENT

Supporting Information

The Supporting Information is available free of charge at https://pubs.acs.org/doi/10.1021/acs.nanolett.2c02792.

Supporting figures, tables and experimental methods (PDF)

AUTHOR INFORMATION

Corresponding Authors

Yi Cui − *Department of Materials Science and Engineering, Stanford University, Stanford, California 94305, United States; Stanford Institute for Materials and Energy Sciences, SLAC National Accelerator Laboratory, Menlo Park, California 94025, United States;* orcid.org/0000-0002-6103-6352; Email: yicui@stanford.edu

https://doi.org/10.1021/acs.nanolett.2c02792
Nano Lett. XXXX, XXX, XXX−XXX

Zhenan Bao − *Department of Chemical Engineering, Stanford University, Stanford, California 94305, United States;* orcid.org/0000-0002-0972-1715; Email: zbao@stanford.edu

Authors

David T. Boyle − *Department of Chemistry, Stanford University, Stanford, California 94305, United States;* orcid.org/0000-0002-0452-275X

Yuzhang Li − *Department of Materials Science and Engineering, Stanford University, Stanford, California 94305, United States; Department of Chemical and Biomolecular Engineering, University of California—Los Angeles, Los Angeles, California 90095, United States*

Allen Pei − *Department of Materials Science and Engineering, Stanford University, Stanford, California 94305, United States;* orcid.org/0000-0001-8930-2125

Rafael A. Vilá − *Department of Materials Science and Engineering, Stanford University, Stanford, California 94305, United States*

Zewen Zhang − *Department of Materials Science and Engineering, Stanford University, Stanford, California 94305, United States;* orcid.org/0000-0002-4909-4330

Philaphon Sayavong − *Department of Chemistry, Stanford University, Stanford, California 94305, United States*

Mun Sek Kim − *Department of Materials Science and Engineering, Stanford University, Stanford, California 94305, United States*

William Huang − *Department of Materials Science and Engineering, Stanford University, Stanford, California 94305, United States;* orcid.org/0000-0001-8717-5337

Hongxia Wang − *Department of Materials Science and Engineering, Stanford University, Stanford, California 94305, United States;* orcid.org/0000-0003-0720-3305

Yunzhi Liu − *Department of Materials Science and Engineering, Stanford University, Stanford, California 94305, United States;* orcid.org/0000-0003-0524-4023

Rong Xu − *Department of Materials Science and Engineering, Stanford University, Stanford, California 94305, United States;* orcid.org/0000-0002-3694-595X

Robert Sinclair − *Department of Materials Science and Engineering, Stanford University, Stanford, California 94305, United States*

Jian Qin − *Department of Chemical Engineering, Stanford University, Stanford, California 94305, United States;* orcid.org/0000-0001-6271-068X

Complete contact information is available at: https://pubs.acs.org/10.1021/acs.nanolett.2c02792

Author Contributions

#D.T.B. and Y.L. contributed equally.

Author Contributions

D.B., Yuz.L., A.P., and Y.C. conceived the study. D.B. designed the electrochemical experiments, collected electroanalytical data, and compiled and analyzed all results. A.P. collected the initial SEM images of faceted Li grown on the UME and analyzed the faceted structures. Yuz.L. collected the cryo-TEM data of faceted Li and interpreted the results with Yun.L. and R.S. R.V., W.H., and Z.Z. helped collect measurements of the SEI thickness with cryo-TEM. P.S. helped design some electrochemical methods and collect SEM images with D.B. H.W. helped prepare TEM grids. R.X. calculated the effect of migration on electrochemical measurements. D.B. wrote the manuscript with input from coauthors and guidance from J.Q., Z.B., and Y.C.

Notes

The authors declare no competing financial interest.

■ ACKNOWLEDGMENTS

We acknowledge support from the Assistant Secretary for Energy Efficiency and Renewable Energy, Office of Vehicle Technologies of the US Department of Energy under the Battery Materials Research (BMR) Program and Battery 500 Consortium. The cryo-TEM research is supported by the Department of Energy, Office of Basic Energy Sciences, Division of Materials Science and Engineering under Contract DE-AC02-76SF00515. D.T.B. acknowledges support from the National Science Foundation Graduate Research Fellowship Program. This work was supported in part by the National Science Foundation under Grant No. CBET-2143677. Scanning electron microscopy and TEM were performed at the Stanford Nano Shared Facilities (SNSF), partially supported by the National Science Foundation under Award ECCS-1542152. The K3 IS camera and support are courtesy of Gatan.

■ REFERENCES

(1) Lin, D.; Liu, Y.; Cui, Y. Reviving the Lithium Metal Anode for High-Energy Batteries. *Nat. Nanotechnol.* **2017**, *12* (3), 194−206.

(2) Boyle, D. T.; Huang, W.; Wang, H.; Li, Y.; Chen, H.; Yu, Z.; Zhang, W.; Bao, Z.; Cui, Y. Corrosion of Lithium Metal Anodes during Calendar Ageing and Its Microscopic Origins. *Nat. Energy* **2021**, *6*, 487−494.

(3) Fang, C.; Li, J.; Zhang, M.; Zhang, Y.; Yang, F.; Lee, J. Z.; Lee, M.; Alvarado, J.; Schroeder, M. A.; Yang, Y.; et al. Quantifying Inactive Lithium in Lithium Metal Batteries. *Nature* **2019**, *572*, 511−515.

(4) Hobold, G. M.; Lopez, J.; Guo, R.; Minafra, N.; Banerjee, A.; Meng, Y. S.; Shao-horn, Y.; Gallant, B. M. Moving beyond 99.9% Coulombic Efficiency for Lithium Anodes in Liquid Electrolytes. *Nat. Energy* **2021**, *6* (10), 951−960.

(5) Niu, C.; Liu, D.; Lochala, J. A.; Anderson, C. S.; Cao, X.; Gross, M. E.; Xu, W.; Zhang, J.; Whittingham, M. S.; Xiao, J.; et al. Balancing Interfacial Reactions to Achieve Long Cycle Life in High-Energy Lithium Metal Batteries. *Nat. Energy* **2021**, *6*, 723−732.

(6) Louli, A. J.; Coon, M.; Genovese, M.; Eldesoky, A.; Dahn, J. R. Optimizing Cycling Conditions for Anode-Free Lithium Metal Cells Optimizing Cycling Conditions for Anode-Free Lithium Metal. *J. Electrochem. Soc.* **2021**, *168*, No. 020515.

(7) Foroozan, T.; Sharifi-asl, S.; Shahbazian-yassar, R. Mechanistic Understanding of Li Dendrites Growth by In- Situ/Operando Imaging Techniques. *J. Power Sources* **2020**, *461*, 228135.

(8) Li, Z.; Huang, J.; Yann Liaw, B.; Metzler, V.; Zhang, J. A Review of Lithium Deposition in Lithium-Ion and Lithium Metal Secondary Batteries. *J. Power Sources* **2014**, *254*, 168−182.

(9) Xiao, J. How Lithium Dendrites Form in Liquid Batteries. *Science (80-.).* **2019**, *366* (6464), 426−428.

(10) Monroe, C.; Newman, J. The Effect of Interfacial Deformation on Electrodeposition Kinetics. *J. Electrochem. Soc.* **2004**, *151* (6), A880−A886.

(11) Barton, J. L.; Bockris, J. O. The Electrolytic Growth of Dendrites from Ionic Solutions. *Proc. R. Soc. A* **1962**, *268* (1335), 485−505.

(12) Chazalviel, J. N. Electrochemical Aspects of the Generation of Ramified Metallic Electrodeposits. *Phys. Rev. A* **1990**, *42* (12), 7355−7367.

(13) Witten, T. A.; Sander, L. M. Diffusion-Limited Aggregation, a Kinetic Critical Phenomenon. *Phys. Rev. Lett.* **1981**, *47* (19), 1400−1403.

(14) Hao, F.; Verma, A.; Mukherjee, P. P. Mesoscale Complexations in Lithium Electrodeposition. *ACS Appl. Mater. Interfaces* **2018**, *10* (31), 26320−26327.
(15) Uppaluri, M.; Subramaniam, A.; Mishra, L.; Viswanathan, V.; Subramanian, V. R. Can a Transport Model Predict Inverse Signatures in Lithium Metal Batteries Without Modifying Kinetics? *J. Electrochem. Soc.* **2020**, *167* (16), 160547.
(16) Hong, Z.; Viswanathan, V. Phase-Field Simulations of Lithium Dendrite Growth with Open-Source Software. *ACS Energy Lett.* **2018**, *3*, 1737−1743.
(17) Bai, P.; Li, J.; Brushett, F. R.; Bazant, M. Z. Transition of Lithium Growth Mechanisms in Liquid Electrolytes. *Energy Environ. Sci.* **2016**, *9*, 3221−3229.
(18) Wu, H.; Jia, H.; Wang, C.; Zhang, J.; Xu, W. Recent Progress in Understanding Solid Electrolyte Interphase on Lithium Metal Anodes. *Adv. Energy Mater.* **2021**, *11*, 2003092.
(19) Peled, E.; Yamin, H. Solid Electrolyte Interphase (SEI) Electrodes. Part 1. The Kinetics of Lithium in LiAICI4-SOCl2. *Isr. J. Chem.* **1979**, *18*, 131−135.
(20) Aurbach, D.*Nonaqueous Electrochemistry*; Dekker, M., Ed.; New York, 1999.
(21) Tikekar, M. D.; Choudhury, S.; Tu, Z.; Archer, L. A. Design Principles for Electrolytes and Interfaces for Stable Lithium-Metal Batteries. *Nat. Energy* **2016**, *1* (9), 1−7.
(22) Wood, K. N.; Kazyak, E.; Chadwick, A. F.; Chen, K. H.; Zhang, J. G.; Thornton, K.; Dasgupta, N. P. Dendrites and Pits: Untangling the Complex Behavior of Lithium Metal Anodes through Operando Video Microscopy. *ACS Cent. Sci.* **2016**, *2* (11), 790−801.
(23) Aurbach, D. Review of Selected Electrode-Solution Interactions Which Determine the Performance of Li and Li Ion Batteries. *J. Power Sources* **2000**, *89* (2), 206−218.
(24) He, M.; Guo, R.; Hobold, G. M.; Gao, H.; Gallant, B. M. The Intrinsic Behavior of Lithium Fluoride in Solid Electrolyte Interphases on Lithium. *Proc. Natl. Acad. Sci. U. S. A.* **2020**, *117*, 73−79.
(25) Wood, K. N.; Noked, M.; Dasgupta, N. P. Lithium Metal Anodes: Toward an Improved Understanding of Coupled Morphological, Electrochemical, and Mechanical Behavior. *ACS Energy Lett.* **2017**, *2*, 664−672.
(26) Maraschky, A.; Akolkar, R. Mechanism Explaining the Onset Time of Dendritic Lithium Electrodeposition via Considerations of the Li + Transport within the Solid Electrolyte Interphase. *J. Electrochem. Soc.* **2018**, *165* (14), D696−D703.
(27) Yang, T.; Li, H.; Tang, Y.; Chen, J.; Ye, H.; Wang, B.; Zhang, Y.; Du, C.; Yao, J.; Guo, B. In Situ Observation of Cracking and Self-Healing of Solid Electrolyte Interphases during Lithium Deposition. *Sci. Bull.* **2021**, *66*, 1754.
(28) Steiger, J.; Richter, G.; Wenk, M.; Kramer, D.; Mönig, R. Comparison of the Growth of Lithium Filaments and Dendrites under Different Conditions. *Electrochem. commun.* **2015**, *50*, 11−14.
(29) Steiger, J.; Kramer, D.; Mönig, R. Mechanisms of Dendritic Growth Investigated by in Situ Light Microscopy during Electrodeposition and Dissolution of Lithium. *J. Power Sources* **2014**, *261*, 112−119.
(30) Zhang, L.; Yang, T.; Du, C.; Liu, Q.; Tang, Y.; Zhao, J.; Wang, B.; Chen, T.; Sun, Y.; Jia, P.; et al. Lithium Whisker Growth and Stress Generation in an in Situ Atomic Force Microscope−Environmental Transmission Electron Microscope Set-Up. *Nat. Nanotechnol.* **2020**, *15* (2), 94−98.
(31) He, Y.; Ren, X.; Xu, Y.; Engelhard, M. H.; Li, X.; Xiao, J.; Liu, J.; Zhang, J. G.; Xu, W.; Wang, C. Origin of Lithium Whisker Formation and Growth under Stress. *Nat. Nanotechnol.* **2019**, *14* (11), 1042−1047.
(32) Kushima, A.; So, K. P.; Su, C.; Bai, P.; Kuriyama, N.; Maebashi, T.; Fujiwara, Y.; Bazant, M. Z.; Li, J. Liquid Cell Transmission Electron Microscopy Observation of Lithium Metal Growth and Dissolution: Root Growth, Dead Lithium and Lithium Flotsams. *Nano Energy* **2017**, *32*, 271−279.
(33) Boyle, D. T.; Kong, X.; Pei, A.; Rudnicki, P. E.; Shi, F.; Huang, W.; Bao, Z.; Qin, J.; Cui, Y. Transient Voltammetry with Ultramicroelectrodes Reveals the Electron Transfer Kinetics of Lithium Metal Anodes. *ACS Energy Lett.* **2020**, *5*, 701−709.
(34) Genders, D.; Hedges, W. M.; Pletcher, D. Application of Microelectrodes to the Study of the Li, Li + Couple in Ether Solvents. *J. Chem. Soc., Faraday Trans.* **1984**, *80*, 3399−3408.
(35) Verbrugge, M. W.; Koch, B. J. Microelectrode Study of the Lithium/Propylene Carbonate Interface: Temperature and Concentration Dependence of Physicochemical Parameters. *J. Electrochem. Soc.* **1994**, *141* (11), 3053−3059.
(36) Odziemkowski, M.; Irish, D. E. An Electrochemical Study of the Reactivity at the Lithium Electrolyte/Bare Lithium Metal Interface I. Purified Electrolytes. *J. Electrochem. Soc.* **1992**, *139* (11), 3063−3074.
(37) Peled, E.; Menkin, S. Review—SEI: Past, Present and Future. *J. Electrochem. Soc.* **2017**, *164* (7), A1703−A1719.
(38) Zhang, Z.; Li, Y.; Zhou, W.; Li, Y.; Oyakhire, S. T.; Boyle, D. T.; Wu, Y.; Xu, J.; Wang, H.; Yu, Z.; et al. Capturing the Swelling of Solid-Electrolyte Interphase in Lithium Metal Batteries. *Science (80-.)* **2022**, *375*, 66−70.
(39) Guo, R.; Gallant, B. M. Li2O Solid Electrolyte Interphase: Probing Transport Properties at the Chemical Potential of Lithium. *Chem. Mater.* **2020**, *32*, 5525−5533.
(40) Lu, P.; Li, C.; Schneider, E. W.; Harris, S. J. Chemistry, Impedance, and Morphology Evolution in Solid Electrolyte Interphase Films during Formation in Lithium Ion Batteries. *J. Phys. Chem. C* **2014**, *118* (2), 896−903.
(41) Shi, S.; Lu, P.; Liu, Z.; Qi, Y.; Hector, L. G.; Li, H.; Harris, S. J. Direct Calculation of Li-Ion Transport in the Solid Electrolyte Interphase. *J. Am. Chem. Soc.* **2012**, *134*, 15476−15487.
(42) Huang, W.; Boyle, D. T.; Li, Y.; Li, Y.; Pei, A.; Chen, H.; Cui, Y. Nanostructural and Electrochemical Evolution of the Solid-Electrolyte Interphase on CuO Nanowires Revealed by Cryogenic Electron Microscopy and Impedance Spectroscopy. *ACS Nano* **2019**, *13* (1), 737−744.
(43) Bard, A. J.; Faulkner, L. R.*Fundamentals and Applications*; John Wiley and Sons, Inc.: NJ, 2001.
(44) Hayamizu, K.; Aihara, Y.; Arai, S.; Martinez, C. G. Pulse-Gradient Spin-Echo 1H, 7Li, and 19F NMR Diffusion and Ionic Conductivity Measurements of 14 Organic Electrolytes Containing LiN(SO2CF3)2. *J. Phys. Chem. B* **1999**, *103* (3), 519−524.
(45) Gunnarsdóttir, A. B.; Vema, S.; Menkin, S.; Marbella, L. E.; Grey, C. P. Investigating the Effect of a Fluoroethylene Carbonate Additive on Lithium Deposition and the Solid Electrolyte Interphase in Lithium Metal Batteries Using: In Situ NMR Spectroscopy. *J. Mater. Chem. A* **2020**, *8* (30), 14975−14992.
(46) Scharifker, B. R.; Mostany, J. Three-Dimensional Nucleation with Diffusion Controlled Growth. Part I. Number Density of Active Sites and Nucleation Rates per Site. *J. Electroanal. Chem.* **1984**, *177* (1−2), 13−23.
(47) Thirumalraj, B.; Hagos, T. T.; Huang, C. J.; Teshager, M. A.; Cheng, J. H.; Su, W. N.; Hwang, B. J. Nucleation and Growth Mechanism of Lithium Metal Electroplating. *J. Am. Chem. Soc.* **2019**, *141*, 18612−18623.
(48) Palomar-Pardavé, M.; Scharifker, B. R.; Arce, E. M.; Romero-Romo, M. Nucleation and Diffusion-Controlled Growth of Electroactive Centers: Reduction of Protons during Cobalt Electrodeposition. *Electrochim. Acta* **2005**, *50* (24), 4736−4745.
(49) Sekerka, R. F. Equilibrium and Growth Shapes of Crystals: How Do They Differ and Why Should We Care? *Cryst. Res. Technol.* **2005**, *40* (4−5), 291−306.
(50) Stottmeister, D.; Groß, A. Strain Dependence of Metal Anode Surface Properties. *ChemSusChem* **2020**, *13*, 3147−3153.
(51) Chang, H. J.; Ilott, A. J.; Trease, N. M.; Mohammadi, M.; Jerschow, A.; Grey, C. P. Correlating Microstructural Lithium Metal Growth with Electrolyte Salt Depletion in Lithium Batteries Using 7Li MRI. *J. Am. Chem. Soc.* **2015**, *137* (48), 15209−15216.
(52) Cao, X.; Ren, X.; Zou, L.; Engelhard, M. H.; Huang, W.; Wang, H.; Matthews, B. E.; Lee, H.; Niu, C.; Arey, B. W.; et al. Monolithic Solid−Electrolyte Interphases Formed in Fluorinated Orthoformate-

https://doi.org/10.1021/acs.nanolett.2c02792
Nano Lett. XXXX, XXX, XXX−XXX

Based Electrolytes Minimize Li Depletion and Pulverization. *Nat. Energy* **2019**, *4* (9), 796−805.
(53) Li, Y.; Li, Y.; Pei, A.; Yan, K.; Sun, Y.; Wu, C. L.; Joubert, L. M.; Chin, R.; Koh, A. L.; Yu, Y.; et al. Atomic Structure of Sensitive Battery Materials and Interfaces Revealed by Cryo−Electron Microscopy. *Science (80-.)* **2017**, *358* (6362), 506−510.
(54) Yu, Z.; Wang, H.; Kong, X.; Huang, W.; Tsao, Y.; Mackanic, D. G.; Wang, K.; Wang, X.; Huang, W.; Choudhury, S.; et al. Molecular Design for Electrolyte Solvents Enabling Energy-Dense and Long-Cycling Lithium Metal Batteries. *Nat. Energy* **2020**, *5* (7), 526−533.
(55) Yu, Z.; Rudnicki, P. E.; Zhang, Z.; Huang, Z.; Celik, H.; Oyakhire, S. T.; Chen, Y.; Kong, X.; Kim, S. C.; Xiao, X.; et al. Rational Solvent Molecule Tuning for High-Performance Lithium Metal Battery Electrolytes. *Nat. Energy* **2022**, *7* (1), 94−106.
(56) Yang, H.; Fey, E. O.; Trimm, B. D.; Dimitrov, N.; Whittingham, M. S. Effects of Pulse Plating on Lithium Electrodeposition, Morphology and Cycling Efficiency. *J. Power Sources* **2014**, *272*, 900−908.
(57) Li, Q.; Tan, S.; Li, L.; Lu, Y.; He, Y. Understanding the Molecular Mechanism of Pulse Current Charging for Stable Lithium-Metal Batteries. *Sci. Adv.* **2017**, *3* (7), 1−10.
(58) García, G.; Dieckhöfer, S.; Schuhmann, W.; Ventosa, E. Exceeding 6500 Cycles for LiFePO4/Li Metal Batteries through Understanding Pulsed Charging Protocols. *J. Mater. Chem. A* **2018**, *6* (11), 4746−4751.

https://doi.org/10.1021/acs.nanolett.2c02792
Nano Lett. XXXX, XXX, XXX−XXX